AIN-based hybrid thin films with selfassembled plasmonic Au and Ag nanoinclusions

Cite as: Appl. Phys. Lett. **114**, 023103 (2019); https://doi.org/10.1063/1.5083950 Submitted: 02 December 2018 . Accepted: 30 December 2018 . Published Online: 16 January 2019

Xuejing Wang, Trang Nguyen, Yang Cao, Jie Jian 🗓, Oana Malis 🗓, and Haiyan Wang 🗓







ARTICLES YOU MAY BE INTERESTED IN

Enhanced quantum dots spontaneous emission with metamaterial perfect absorbers Applied Physics Letters 114, 021103 (2019); https://doi.org/10.1063/1.5081688

The role of transient surface morphology on composition control in AlGaN layers and wells Applied Physics Letters 114, 031602 (2019); https://doi.org/10.1063/1.5063933

Carrier localization structure combined with current micropaths in AlGaN quantum wells grown on an AlN template with macrosteps

Applied Physics Letters 114, 011102 (2019); https://doi.org/10.1063/1.5063735

Applied Physics Reviews
Now accepting original research

2017 Journal Impact Factor: 12.894



AIN-based hybrid thin films with self-assembled plasmonic Au and Ag nanoinclusions

Cite as: Appl. Phys. Lett. **114**, 023103 (2019); doi: 10.1063/1.5083950 Submitted: 02 December 2018 · Accepted: 30 December 2018 · Published Online: 16 January 2019







Xuejing Wang, Trang Nguyen, Yang Cao, Jie Jian, Dana Malis, Dand Haiyan Wang (13,a)

AFFILIATIONS

- ¹ Department of Materials Engineering, Purdue University, West Lafayette, Indiana 47907, USA
- Department of Physics and Astronomy, Purdue University, West Lafayette, Indiana 47907, USA
- Department of Electrical Engineering, Purdue University, West Lafayette, Indiana 47907, USA
- a) Author to whom correspondence should be addressed: hwang00@purdue.edu

ABSTRACT

Aluminum nitride (AlN)-based two-phase nanocomposite thin films with plasmonic Au and Ag nanoinclusions have been demonstrated using a one-step thin film growth method. Such AlN-based nanocomposites, while maintaining their wide bandgap semiconductor behavior, present tunable optical properties such as bandgap, plasmonic resonance, and complex dielectric function. Depending on the growth atmosphere, the metallic nanoinclusions self-organized into different geometries, such as nanodendrites, nano-disks, and nanoparticles, providing enhanced optical anisotropy in-plane and out-of-plane. The infrared transmission measurements demonstrate the signature peaks of AlN as well as a broad transmission window attributed to the plasmonic nanoinclusions. This unique AlN-metal hybrid thin film platform provides a route to modulate the optical response of wide bandgap III-V nitride semiconductors towards infrared sensing or all optical based integrated circuits.

Published under license by AIP Publishing. https://doi.org/10.1063/1.5083950

Plasmonic nanostructures are known for their outstanding properties in manipulating light-matter interactions, due to surface plasmon polaritons (SPRs) and localized surface plasmon resonance (LSPR). The famous example of Lycurgus cup with Au nanoparticle (NP) color centers has been known for centuries and opens the route for artificial (meta)material designs in combining metallic nanostructures in different material media for multi-functionalities. With a pronounced difference in electromagnetic parameters, metal-dielectric combination on the nanoscale is of great interest. It induces SPRs that have various applications, including photovoltaic and photocatalytic devices,² bio-medical sensing,³ integrated nanophotonic circuits,⁴ etc. From the materials science perspective, the metal-dielectric metamaterial can be termed nanocomposites, namely, two- or multi-phase materials that are physically or/and chemically fabricated into a whole unit. Limited success has been achieved in areas of metal-oxide hybrid thin film systems.^{5,}

Wide bandgap semiconductors, especially the III-V nitride family including GaN, AlN, and their alloys, have been widely explored for optoelectronic devices such as solid state lasers, solid state lighting, and photovoltaics, as well as high power electronics.^{7–9} On the other hand, research directions on

exploring new materials towards future all optical based integrated circuits excite the community in search of various materials with a wide range of optical tunabilities. An effective approach is to combine the plasmonic nanostructure designs with nitride based dielectric materials to achieve such tunability. Very recently, an initial demonstration of the epitaxial growth of vertically aligned nanocomposites of metal-transition metal nitrides, such as Au-TaN or Ag-TiN, ^{10,11} has suggested the possibilities of integrating such dissimilar materials together in a hybrid material form. However, such integration focused on two plasmonic systems with limited tunabilities of dielectric function. It is expected that incorporating metallic nanoinclusions into dielectric III-V nitride systems could present a large range of optical tunabilities, especially the complex dielectric functions in a wide optical range. However, such demonstration is very challenging and has not yet been realized, largely due to the complexity under different growth conditions of metal and III-V nitrides as well as their lattice compatibility, as plasmonic metals mostly have FCC structures, while III-V nitrides are wurtzite (hexagonal close packed).

In this work, we demonstrate the possibility of incorporating plasmonic Au and Ag nanoinclusions in III-V nitrides with

various geometries. As a model system, we selected AlN as the matrix material for this demonstration. AlN presents a wide bandgap of ~6 eV and has been widely incorporated in III-V-based optoelectronic devices as an effective buffer for GaN growth and alloy components for bandgap tuning. ^{12–14} AlN has also shown piezoelectric properties for MEMS, ¹⁵ microwave (GHz) filters, ^{16,17} and other optical capabilities. ^{18,19} These unique properties make AlN an ideal candidate for optoelectronic based applications as compared to most oxides. By careful control of the growth conditions, the Au and Ag nanoinclusions in AlN present various geometries and offer pronounced tunabilities in bandgap, optical absorption, dielectric function and anisotropy, as well as plasmon resonance in the mid-infrared range. Furthermore, such hybrid systems can also be integrated on Si substrates for Fourier transform infrared spectroscopy (FTIR) measurements demonstrated in this work.

The films were deposited using a pulsed laser deposition (PLD) system with a KrF excimer laser (Lambda Physik Compex Pro 205, $\lambda = 248$ nm). The laser beam was focused onto the target with an incident angle of 45° and an energy density of around 3.5 J/cm^2 . The chamber was initially pumped to 1.0×10^{-6} mbar. The thin film depositions were carried out under 10-15 Hz and at the temperature of 700 °C on both c-cut sapphire and (001) Si substrates. For Si substrates, 5% HF solution was applied to remove the surface oxide layer before deposition. After the deposition, the chamber was automatically cooled to room temperature under vacuum. It is noted that the metal:AIN ratio in the composite target is controlled with the weight ratio of 3:97, which results in the atomic ratio of \sim 12.94 at. % for Au and \sim 7.53 at. % for Ag, respectively. The microstructures of deposited films were characterized by X-ray diffraction θ -2 θ (Panalytical X'Pert X-ray diffractometer, Cu K_{α} radiation), bright field transmission electron microscopy (TEM, FEI Talos F200X TEM) high-angle annular dark field (HAADF) scanning (S)TEM images, selected area electron diffraction (SAED) patterns, and energy-dispersive X-ray spectroscopy (EDS) chemical mappings. The TEM samples were prepared using a standard cross-section sample preparation procedure, including manual grinding, dimpling, and ion milling (PIPS 691 precision ion polishing system, 4.0 keV).

The transport properties of as-deposited films were measured by a standard four probe method with the temperature varying from 5 K to 390 K in a physical property measurement system (PPMS, Quantum Design). Normal incident depolarized transmittance (T%) and reflectivity (R%) spectra were recorded using an UV-Vis spectrophotometer (Lambda 1050 UV/Vis spectrophotometer). Ellipsometry experiments were carried out on a RC2 spectroscopic ellipsometer (J.A. Woollam Company). Three angles 30°, 45°, and 60° and a spectral range from 210 to 2500 nm were covered for the measurements. Fourier transform infrared (FTIR) spectra were measured (using a Nicolet 8700 FT-IR spectrometer, Fisher Scientific) at room temperature, with the input polarizer fixed at either 0° (p-pol) or 90° (s-pol). A high sensitivity mercury cadmium telluride (MCT) detector and an indium antimonide (InSb) detector were used for mid-IR and near-IR range, respectively. The FTIR samples were prepared by mechanical polishing with the sample mounted on a 45° sample holder for the wedge angle.

To identify the growth orientation and the crystalline quality of metal-AlN hybrid thin films, the as-grown AlN/sapphire, Au-AlN/sapphire, and Ag-AlN/sapphire thin film samples were characterized using XRD. The θ -2 θ scans from 32 to 45 $^{\circ}$ were collected and displayed separately in Fig. 1. Pure AlN (a) grown on c-cut sapphire exhibits a strong (0002) h-AlN peak at 35.735°, which is close to other literature reports.²⁰ On the other hand, multiple peaks have been observed in the nanocomposite samples (b) and (c), where (111) Au at 38.220°, (111) Ag at 38.117°, and a weak (002) Ag at 44.334° are identified. Such strong and sharp metal peaks indicate good crystallinity as well as clear phase separation of the metallic phase. Meanwhile, the (0002) AlN growth is suppressed as seen from a broader (0002) AlN peak and an additional peak at 40.41° in the Au-AlN nanocomposite film. The (0002) AlN position remains almost identical in three samples (~35.7°), which indicates that the interfacial strain between AlN and the sapphire substrate is unaffected by introducing a secondary phase, and (0002) AlN is expected to dominate the initial thin film growth.

The microstructures were further explored using (Scanning) Transmission Electron Microscopy [(S)TEM]; the STEM images are coupled with selected area diffraction patterns (SAEDs) from the $\langle 1\bar{1}00 \rangle$ zone axis. The pure AlN film, in Fig. 1(d), shows a columnar growth as typically seen in AlN with a sharp film-substrate interface. As is expected, Au-AlN [Fig. 1(e)] and Ag-AlN [Fig. 1(f)] are self-assembled into two phases. Clear diffraction patterns (DPs) indicate the high epitaxial quality of the films. Interestingly, their morphologies are vastly different. With the same metal density, Au nanoinclusions are dendriticlike nanostructures [as illustrated in Fig. 1(e)] which are very fine and dispersed, while Ag adatoms agglomerated into "nanodisks" with sharp boundaries. Careful comparisons of the STEM images indicate that in the initial (~15 nm) growth stage, both Au and Ag appear as very fine particles with a well-ordered arrangement within AlN. These particles are grown as seeds to direct the self-assembling process and phase separation in the later growth stage. Referring to the XRD results, one can observe that there is about 14.25% interfacial strain between (0002) AlN $(2\theta = 35.735^{\circ})$ and (0006) sapphire $(2\theta = 41.672^{\circ})$, which means that the initial AIN layer could be highly strained. Therefore, it is possible that the well-ordered Au (Ag) nanoinclusions serve to compensate the large strain between AlN and the sapphire substrate in the initial growth stage. Once the films reach their critical thickness, a self-organized growth of the metallic phases, either as dendritic-like or disk-like nanostructures, starts in the second stage. In the second stage, the morphologies largely result from different surface energies between the metal and AlN and the growth kinetics. The surface morphology of the two nanocomposites was further examined using scanning electron microscopy (SEM). As is seen from Fig. S1, Au and Ag agglomerated with uniform distribution on the top surface, which could be important for potential applications such as light harvesting or enhanced Raman sensing. Besides the films grown in vacuum, we explored the nanocomposite growth in the backpressure of N2 (50 mTorr) for both Au-AlN and Ag-AlN on sapphire. The TEM and EDS results are displayed in Fig. S2. Under a N₂ atmosphere, both Au and Ag self-organize into much

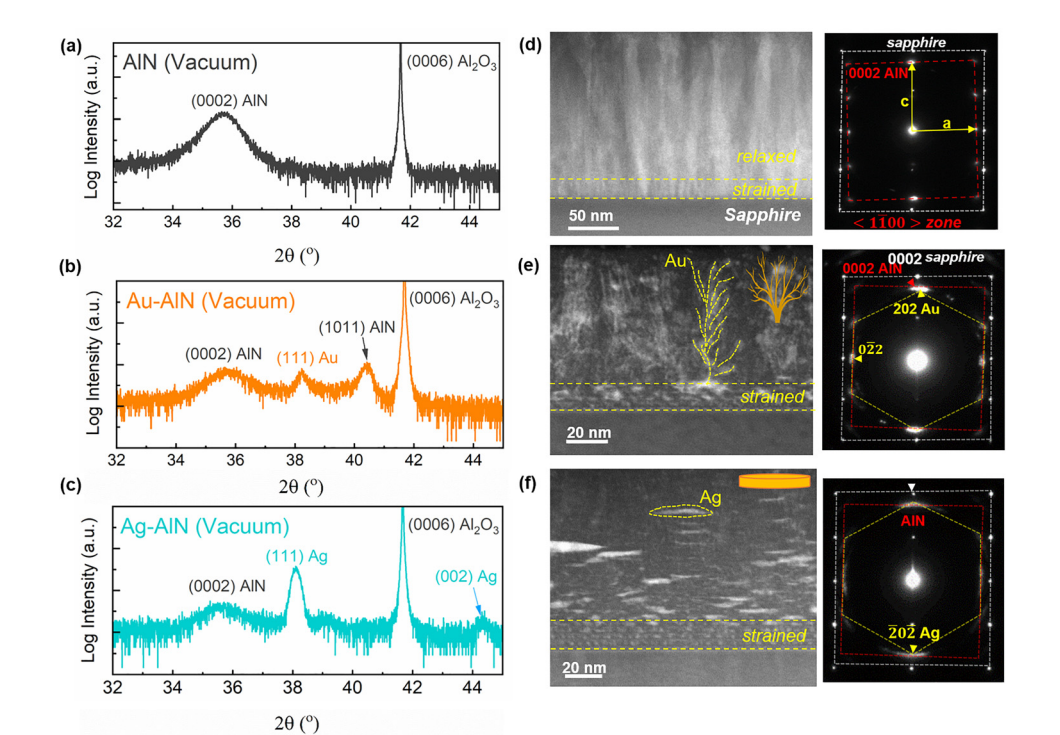


FIG. 1. XRD θ -2 θ scans of vacuum grown films: (a) AIN, (b) Au-AIN and (c) Ag-AIN on a c-cut sapphire substrate. HAADF-STEM images (left) and the corresponding SAED patterns of (d) AIN on sapphire, (e) Au-AIN on sapphire and (f) Ag-AIN on sapphire. Samples were viewed from the $\langle 1100 \rangle$ zone axis.

more confined nanoparticles (NPs). These results suggest that growth morphologies are largely controlled by the growth kinetics during the deposition.

Self-organized Au and Ag nanoinclusions acting as plasmonic resonators inside AlN are expected to tune the overall physical properties. A set of optical transmittance (T%) and reflectance (R%) measurements from 200 to 1500 nm was performed on all five samples: AlN, Au-AlN (vacuum), Ag-AlN (vacuum), Au-AlN (N2), and Ag-AlN (N2). Compared to pure AlN [Fig. (2a)], the attenuated transmittance ((30%)) intensities of the nanocomposite films contribute to the strong absorption at the resonance frequency and enhanced reflectance intensities (~35%) of the metallic phases. Specifically, plasmonic resonance is estimated from the absorbance spectra (A=1-R-T), [Fig. 2(c)], with Au at 352 nm and Ag at 445 nm; the variations of the resonance are mainly affected by the nanoinclusion morphology and are overall consistent with other reported values.2 According to the T% spectra [Fig. 2(a)], the Tauc plot was applied to retrieve the bandgaps of three samples, and $(\alpha hv)^2$ as a function of photon energy is plotted in Fig. 2(b). From the Tauc plot, bandgap tuning is effectively achieved by adding the metallic nanoinclusions. The bandgap of the AlN thin film is 5.36-5.48 eV, while Au-AlN and Ag-AlN are both reduced to 4.63-4.72 eV and 4.76-4.85 eV, respectively. Such optical tuning is possibly related to the change in the charge carrier density in the systems because of metallic nanoinclusions. Electrical transport measurements were conducted on samples in a temperature range from 3 K to 390 K. Figure 2(d) shows the resistivity versus temperature (3 K-390 K) plot. Both Au-AlN and Ag-AlN films show obvious semiconductor behavior but with much enhanced conductivity (AlN, not shown here, is out of range in the transport measurement). The optical and electrical transport properties of the nanocomposites grown in N_2 are shown in Fig. S4, where more ordered nanoparticles exhibit pronounced plasmonic resonance, namely, the 440 nm of Ag NPs and 540 nm of

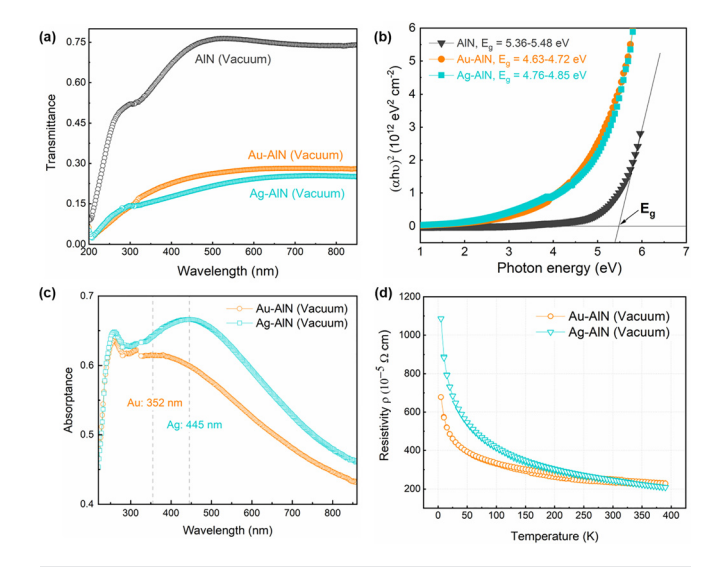


FIG. 2. (a) Transmittance spectra of pure AIN, Au-AIN, and Ag-AIN films grown under vacuum conditions. (b) *Tauc* plot of the bandgap. (c) Absorptance spectra of the two nanocomposites, calculated from A = 1 - R - T. (d) Resistivity versus temperature curves of Au-AIN and Ag-AIN films; note that pure AIN resistivity is out of range.

Au NPs that are consistent with reported studies.²¹ Note that variations of T% of films grown in different environments are due to the geometry and the dimension of nano-inclusions. For example, the dendritic Au as compared to Au NPs are rather dispersed, such that the plasmonic resonance is blue-shifted and the overall extinction is higher.

Ellipsometry parameters (Ψ, Δ) in a broad spectrum range (210-2500 nm) were collected to retrieve effective optical parameters. The addition of a secondary phase breaks the overall symmetry of the hybrid films, and the fitting models were treated as anisotropic models such that the in-plane (ordinary) and out-of-plane (extra-ordinary) parameters can be specified (Fig. 3). Comparing the anisotropic dielectric constants in the two films with Au and Ag nanoinclusions, we observe a significant difference between the ordinary (||) and extraordinary (\perp) values. Specifically, the nano-dendritic Au-AlN one with out-ofplane Au nanoinclusions induces more optical oscillations in the perpendicular direction, represented by a much larger ε₁[⊥] value [Figs. 3(a) and 3(b)]. On the other hand, Ag-AlN with Ag nanodisks exhibits a stronger metallic property in-plane as seen from its lower $\varepsilon_1^{\parallel}$ and larger $\varepsilon_2^{\parallel}$ values [Figs. 3(c) and 3(d)]. The isotropic optical parameters of pure AlN and nanocomposite films are displayed in Fig. S3. Again, with plasmonic metallic nanoinclusions, the films are still semiconducting ($\varepsilon_1 > 0$) in the measured spectrum range, but with a much broader range of dielectric tuning as a function of the wavelength [Fig. S3(b)]. The decreased real part of the dielectric constants (E1) in a lower wavelength range (300-1200 nm) is mainly affected by the metallic nanoinclusions, while the films behave more dielectric in the near-infrared regime (NIR). Detailed ellipsometric parameters and fitted optical constants of Au-AlN (N2) and Ag-AlN (N2) are shown in Fig. S4 in the supplementary material.

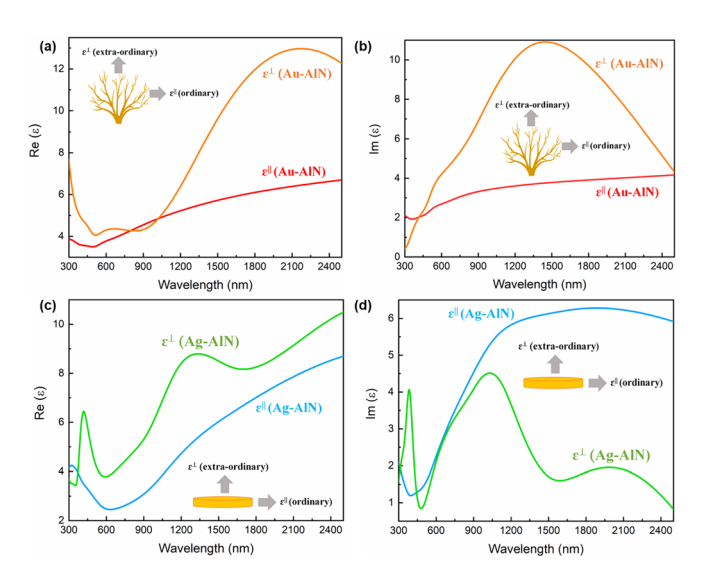


FIG. 3. Optical parameters of ε_1 of Au-AlN and Ag-AlN films grown in vacuum. (a) Anisotropic ε_1 of Au-AlN and (b) the corresponding ε_2 values. (c) Anisotropic ε_1 of Ag-AlN and (d) the corresponding ε_2 values; inset images illustrate the in-plane (||) and out-of-plane (\perp) directions with respect to the Au and Ag geometries.

The infrared (IR) properties of metal-AlN hybrid films (vacuum grown) were further investigated using FTIR. The measurements were conducted using a transmission setup with a built-in polarizer (s-pol and p-pol). Here, the two edges of the thin film samples were polished to wedge angles (45°) to allow multiple bounces in the film, such that light-matter interactions would be strong for enhanced signals. As illustrated in Fig. 4 (insets), the number of bounces inside the sample is calculated using

$$N = l \div t$$
,

where l is the width of the polished sample and t is the sample (film and substrate) thickness. For more accurate comparison, we controlled the number of bounces of all the measured samples (N \sim 6), and the resultant spectra in Fig. 4 are calculated from

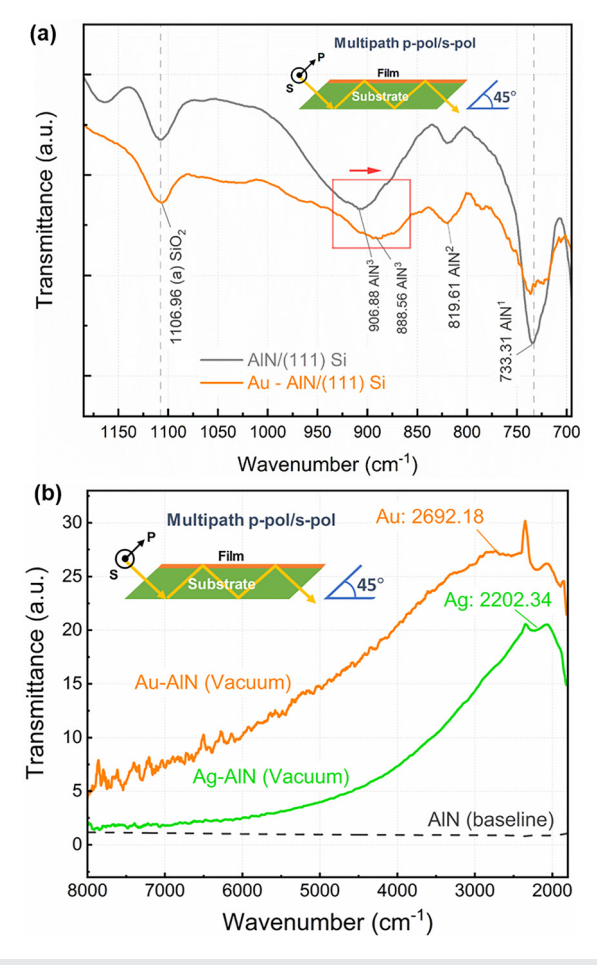


FIG. 4. (a) Mid-IR transmittance spectra of AIN/Si and Au-AIN/Si samples grown in vacuum; the inset shows the illustration of the optical path through the sample. (b) Transmittance spectra in the near-IR range of Au-AIN/sapphire and Ag-AIN/sapphire, and the AIN spectrum is applied as a baseline. Note that the transmittance is taken from the ratio of p-pol intensity/s-pol intensity.

$$T = \frac{T_{sample}^{p-pol}}{T_{background}^{p-pol}} \div \frac{T_{sample}^{s-pol}}{T_{background}^{s-pol}}.$$

The mid-IR spectra were collected for films grown on (111) Si substrates due to the wide transparency range of Si (1.2 μ m–15 μ m). Transmittance spectra of AlN/Si and Au-AlN/Si samples are shown in Fig. 4(a). The strong dip at \sim 733.31 cm⁻¹ is assigned to the E₁ (TO) mode of AlN (active phonon mode), and a wider dip at 906.88 cm⁻¹ (AlN/Si) and 888.56 (Au-AlN/Si) corresponds to the A₁ (LO) mode of AlN, namely, the longitudinal optic phonons.²² Note that a minor shift (\sim 18 cm⁻¹) is related to the Au addition. A weak dip at \sim 819.61 cm⁻¹ corresponding to the E₁ (LO) mode is caused by the cubic-AlN phase, and another defect at \sim 1106 cm⁻¹ belongs to a very thin amorphous SiO₂ layer on the (111) Si substrate. Next, the spectra at near-IR were collected for films grown on c-cut sapphire. In this regime, we are more interested to observe any signatures from the plasmonic counterparts. Therefore, the pure AlN spectrum is applied as background for the Au-AlN and Ag-AlN nanocomposite films. Figure 4(b) shows the spectra after baseline correction, where a pronounced transmission window is observed, with peak positions at 2692.18 cm⁻¹ for Au and 2202.34 cm⁻¹ for Ag. The sharper resonance of Ag is possibly due to a more confined geometry (nano-disks) as compared to relatively dispersed Au nanostructures. This infrared transmission window is correlated with the accumulative scattering effect and/or the higher order surface plasmon polariton (SPP) modes from the dispersed Au (Ag) nanoinclusions.²³ Such unique properties demonstrate tunable IR resonance and can be further explored for potential sensing applications.

In this work, a two-phase plasmonic metamaterial system of metal-AlN with plasmonic Au and Ag nanoinclusions has been demonstrated. Different nanoscale morphologies including dendritic-like Au and disk-like Ag have been formed under high vacuum growth, while under N2, uniform nanoparticles are selforganized in AlN. Based on the hybrid film geometries, optical spectra, coupled with electrical transport (R-T) measurements, demonstrate effective bandgap tuning, a change of electronic states, as well as enhanced absorption attributed to plasmonic color-centers. The two-phase nanocomposites exhibit obvious optical anisotropy in terms of effective dielectric constants, while maintaining their semiconductor nature. We further tested the IR transmission property and identified the (LO), (TO) AlN signature peaks (dips) in both pure AlN and Au-AlN films. In addition, plasmonic inclusions enable a broad transmission window in the mid-IR range of nanocomposites. This initial demonstration of plasmonic nanoinclusions in III-V nitrides presents a unique platform for designing metal-semiconductor metamaterials for optoelectronics and all optical-based integrated circuits on sapphire or Si substrates.

See supplementary material for SEM EDS elemental mappings and ellipsometry fitted optical parameters for Au (Ag)-AlN films grown under vacuum and detailed microstructures and optical properties of Au (Ag)-AlN films grown under a $N_{\rm 2}$ atmosphere.

This work was partially supported by the College of Engineering Start-up Fund and Basil R. Turner Professorship at Purdue University. The atomic scale TEM/STEM imaging effort was funded by the U.S. National Science Foundation (DMR-1565822). X.W. and H.W. acknowledge the support from the U.S. National Science Foundation (DMR-1809520).

REFERENCES

¹D. J. Barber and I. C. Freestone, Archaeometry **32**, 33 (1990).

²C. Clavero, Nat. Photonics 8(2), 95 (2014).

³J. N. Anker, W. P. Hall, O. Lyandres, N. C. Shah, J. Zhao, and R. P. Van Duyne, Nat. Mater. 7(6), 442 (2008).

⁴Y. R. Fang and M. T. Sun, Light: Sci. Appl. **4**(6), e294 (2015).

⁵S. Misra, L. Li, J. Jian, J. Huang, X. Wang, D. Zemlyanov, J.-W. Jang, F. H. Ribeiro, and H. Wang, ACS Appl. Mater. Interfaces **10**(38), 32895–32902 (2018).

⁶J. Huang, T. Jin, S. Misra, H. Wang, Z. Qi, Y. Dai, X. Sun, L. Li, J. Okkema, H.-T. Chen, P.-T. Lin, X. Zhang, and H. Wang, Adv. Opt. Mater. **6**, 1800510 (2018).

⁷C. Edmunds, L. Tang, M. Cervantes, M. Shirazi-Hd, J. Shao, A. Grier, A. Valavanis, J. D. Cooper, D. Li, G. Gardner, D. N. Zakharov, Z. Ikonic, D. Indjin, P. Harrison, M. J. Manfra, and O. Malis, Phys. Rev. B **88**(23), 235306 (2013).

⁸F. A. Ponce and D. P. Bour, Nature **386**(6623), 351 (1997).

⁹Y. Taniyasu, M. Kasu, and T. Makimoto, Nature **441**(7091), 325 (2006).

¹⁰J. Huang, X. Wang, N. L. Hogan, S. Wu, P. Lu, Z. Fan, Y. Dai, B. Zeng, R. Starko-Bowes, J. Jian, H. Wang, L. Li, R. P. Prasankumar, D. Yarotski, M. Sheldon, H. T. Chen, Z. Jacob, X. Zhang, and H. Wang, Adv. Sci. 5(7), 1800416 (2018).

¹¹X. Wang, J. Jian, Z. Zhou, C. Fan, Y. Dai, L. Li, J. Huang, J. Sun, A. Donohue, P. Bermel, X. Zhang, H.-T. Chen, and H. Wang, Adv. Opt. Mater. (published online 2018).

¹²B. Padavala, C. D. Frye, X. J. Wang, Z. H. Ding, R. F. Chen, M. Dudley, B. Raghothamachar, P. Lu, B. N. Flanders, and J. H. Edgar, Cryst. Growth Des. 16(2), 981 (2016).

¹³R. F. Davis, Proc. IEEE **79**(5), 702 (1991).

¹⁴S. Zhao, A. T. Connie, M. H. Dastjerdi, X. H. Kong, Q. Wang, M. Djavid, S. Sadaf, X. D. Liu, I. Shih, H. Guo, and Z. Mi, Sci. Rep. 5, 8332 (2015).

¹⁵K. Tonisch, V. Cimalla, C. Foerster, H. Romanus, O. Ambacher, and D. Dontsov, Sens. Actuators, A 132(2), 658 (2006).

¹⁶H. Okano, N. Tanaka, Y. Takahashi, T. Tanaka, K. Shibata, and S. Nakano, Appl. Phys. Lett. **64**(2), 166 (1994).

¹⁷M. A. Dubois and P. Muralt, Appl. Phys. Lett. **74**(20), 3032 (1999).

¹⁸T. Prokofyeva, M. Seon, J. Vanbuskirk, M. Holtz, S. A. Nikishin, N. N. Faleev, H. Temkin, and S. Zollner, Phys. Rev. B 63(12), 125313 (2001).

¹⁹C. Edmunds, J. Shao, M. Shirazi-Hd, M. J. Manfra, and O. Malis, Appl. Phys. Lett. **105**(2), 021109 (2014).

²⁰K. Jagannadham, A. K. Sharma, Q. Wei, R. Kalyanraman, and J. Narayan, J. Vac. Sci. Technol. A 16(5), 2804 (1998).

²¹K. L. Kelly, E. Coronado, L. L. Zhao, and G. C. Schatz, J. Phys. Chem. B 107(3), 668 (2003).

²²J. Ibanez, S. Hernandez, E. Alarcon-Llado, R. Cusco, L. Artus, S. V. Novikov, C. T. Foxon, and E. Calleja, J. Appl. Phys. **104**(3), 033544 (2008).

²³Y. C. Chen, Y. T. Chang, H. H. Chen, F. T. Chuang, C. H. Cheng, and S. C. Lee, IEEE Photonics Technol. Lett. 25(1), 47 (2013).